Observing carbon dioxide emissions over China's cities and industrial areas with the Orbiting Carbon Observatory-2

Bo Zheng[1], Frederic Chevallier[1], Philippe Ciais[1], Gregoire Broquet[1], Yilong Wang[1,2], Jinghui Lian[1], and Yuanhong Zhao[1]

[1]Laboratoire des Sciences du Climat et de l'Environnement, CEA-CNRS-UVSQ, UMR8212, Gif-sur-Yvette, France
[2]Key Laboratory of Land Surface Pattern and Simulation, Institute of Geographical Sciences and Natural Resources Research, Chinese Academy of Sciences, Beijing, China

Correspondence to: Bo Zheng (bo.zheng@lsce.ipsl.fr)

Abstract. In order to track progress towards the global climate targets, the parties that signed the Paris Climate Agreement will regularly report their anthropogenic carbon dioxide (CO_2) emissions based on energy statistics and CO_2 emission factors. Independent evaluation of this self-reporting system is a fast-growing research topic. Here, we study the value of satellite observations of the column CO_2 concentrations to estimate CO_2 anthropogenic emissions with five years of the Orbiting Carbon Observatory-2 (OCO-2) retrievals over and around China. With the detailed information of emission source locations and the local wind, we successfully observe CO_2 plumes from 46 cities and industrial regions over China and quantify their CO_2 emissions from the OCO-2 observations, which add up to a total of 1.3 Gt CO_2 yr^{-1} that account for approximately 13% of mainland China's annual emissions. The number of cities whose emissions are constrained by OCO-2 here is three to ten times larger than previous studies that only focused on large cities and power plants in different locations around the world. Our satellite-based emission estimates are broadly consistent with the independent values from China's detailed emission inventory MEIC, but are more different from those of two widely used global gridded emission datasets (i.e., EDGAR and ODIAC), especially for the emission estimates for the individual cities. These results demonstrate some skill in the satellite-based emission quantification for isolated source clusters with the OCO-2, despite the sparse sampling of this instrument not designed for this purpose. This skill can be improved by future satellite missions that will have a denser spatial sampling of surface emitting areas, which will come soon in the early 2020s.

1 Introduction

The Paris Agreement on climate change requires all parties (countries) to report their anthropogenic greenhouse gas emissions and removals at least every two years within an enhanced transparency framework (UNFCCC, 2018). Then, starting in 2023, the country reports will periodically form the basis for a global stocktake that will assess collective progress in bringing the global greenhouse gas emissions consistent with global warming well below 2°C above pre-industrial levels. In order to address potential biases in this self-reporting mechanism, the contribution of independent observation systems is being increasingly

30 sought (IPCC, 2019). Our focus here is on the direct observation of fossil fuel carbon dioxide (CO_2) emission plumes from space and on the quantification of CO_2 emissions from this observation independently.

NASA's second Orbiting Carbon Observatory (OCO-2) polar satellite (Eldering et al., 2017) is one of the best existing instruments for the retrieval of column-averaged dry-air mole fraction of CO_2 (XCO_2). It observes the clear-sky and sun-lit part of the Earth with footprints of a few km^2 (1.29 km × 2.25 km) gathered in a ~10 km wide swath for each orbit, particularly

35 suitable for informing natural CO_2 budgets at the continental scales. It has already acquired more than five years of science data since its launch in July 2014, which has provided initial insight into carbon fluxes from the tropical terrestrial ecosystems (Liu et al., 2017; Palmer et al., 2019) but not without ambivalence due to likely significant residual systematic errors in the OCO-2 XCO_2 retrievals (Chevallier, 2018).

Extending the use of OCO-2 to monitor fossil fuel CO_2 emissions is rather challenging because the excess XCO_2 generated by

40 large cities or power plants typically reaches ~ 1% at best (Kort et al., 2012), which is about 4 ppm compared with an instrument noise typically around 0.3–0.6 ppm (Worden et al., 2017) for a single sounding. This non-negligible noise in the XCO_2 retrievals is hardly balanced by the amount of data sampled near emission sources with a narrow swath, which hampers the detection of emission plumes and the precision of emission quantification. Only under rare occasions, the OCO-2 tracks cross CO_2 plumes downwind large cities (Labzovskii et al., 2019; Reuter et al., 2019) or power plants (Schwandner et al., 2017;

45 Nassar et al., 2017; Zheng et al., 2019), limiting the possibility to quantify the corresponding CO_2 emissions to few cases within a year. So far, studies on the potential of spaceborne CO_2 observations to infer CO_2 emissions from large cities or power plants have relied on Observing System Simulation Experiments (OSSEs) (Bovensmann et al., 2010; O'Brien et al., 2016; Broquet et al., 2018; Kuhlmann et al., 2019; Wang et al., 2020) and on several well-chosen cases with real OCO-2 retrievals (Nassar et al., 2017; Reuter et al., 2019; Zheng et al., 2019; Wu et al., 2020). To our knowledge, no attempt has been made yet

50 to infer anthropogenic emissions from actual OCO-2 data over a large area or a long period to evaluate a large-scale CO_2 budget.

Here we analyze all OCO-2 ground tracks between September 2014 and August 2019 over and around China, which is the largest emitter country in the world, in order to quantify CO_2 anthropogenic emissions at a large spatial extent over China. We develop a novel, simple, and effective approach to identify the CO_2 plumes from isolated emission clusters, to relate them

55 unambiguously to nearby human emission sources, and to estimate the CO_2 emission fluxes causing each plume. The five-year period allows nearly one-sixth of all the emissions from mainland China to be observed, although OCO-2 swaths have a low probability to cross the emission plume from a given city. The budget of CO_2 emissions aggregating all the sources inferred from the satellite is compared to different emission inventories compiled by multiplying fuel consumption statistics by emission factors. Such a comparison, for the first time covering a significant fraction of the emissions from a country,

60 demonstrates the potential of independently evaluating the self-reporting emission inventories from space.

2 Data and Method

2.1 Data input

We use version 9r of the OCO-2 bias-corrected XCO_2 retrievals (Kiel et al., 2019). We use the good quality data (xco2_quality_flag equals 0) over both land and ocean, and associated retrieval uncertainty statistics. Our inversion framework relies on auxiliary information about winds and about the spatial distribution of emission sources, which are jointly used to link the observed CO_2 plume section with upwind local emission sources. We choose the spatially explicit Multi-resolution Emission Inventory for China (MEIC) dataset (Zheng et al., 2018a, 2018b) that provides the locations of ~100,000 individual industrial point sources (82% of mainland China emissions) and 0.1°×0.1° area source emissions (18% of mainland China emissions) developed for the year 2013. Unlike other inventories used to map industrial emissions using spatial proxies, MEIC includes local reports from each power plant and industrial operator about their emissions and geographic locations. The ERA5 reanalysis data (C3S, 2017) provides us with a first guess for the local wind fields.

2.2 OCO-2 XCO_2 local enhancement

The key steps of our method are the identification of an XCO_2 local enhancement from the satellite data that can be attributed to a CO_2 plume from a large emission source, its separation from the surrounding background, and the establishment of a numerical link to the nearby upwind human emission sources. They are designed to account for the specificity of the sampling capability of OCO-2 and for the XCO_2 retrieval errors.

First, we look for XCO_2 anomalies along the OCO-2 tracks, which exceed 2 sigmas of the spatial variability above the local average within 200-km wide moving windows centered on the locations of the anomalies. These anomalies potentially belong to significant CO_2 plumes. In each window corresponding to such an anomaly and with more than 200 high-quality retrievals (with ~800 retrievals if none are missing due to cloud contaminations or other issues in the retrieval algorithm), the following curve fitting is applied to the XCO_2 retrieval data along the OCO-2 track:

$$y = m \cdot x + b + \frac{A}{\sigma\sqrt{2\pi}} e^{\left[-(x-\mu)^2 \Big/ 2\sigma^2 \right]} \tag{1}$$

where y is XCO_2 (ppm), x is the distance (km) along the OCO-2 track in a fitting window, $m, b, A, \mu,$ and σ are parameters that determine the curve shape, estimated by a nonlinear least-squares fit weighted by the reciprocal of XCO_2 uncertainty statistics. The linear part $m \cdot x + b$ represents the background level assuming the background is linear (Reuter et al., 2019), while the remaining part depicts a single XCO_2 peak with a Gaussian shape (Nassar et al., 2017). Several XCO_2 anomalies should belong to the same CO_2 plume: in order to only define a single equation for a given plume and the corresponding background, we fit the curve around each XCO_2 anomaly and select the one with the largest R^2. We also reject all cases with low R^2 (less than 0.25) to achieve better fitting performance.

Second, we select the cases when the range of $\mu \pm 3\sigma$ is fully covered by the 200-km window to achieve complete fitting curves that cover both the plume part and the wide range of local background. To make the curve fitting robust, we further select the

observational cases that have at least 3 valid cross-track footprints (8 footprints if none is missing) on average within the plume transect ($\mu \pm 2\sigma$) to constrain the shape of the fitted curve with enough data points. Finally, we check if the parameter A is positive and if the average XCO_2 value within the plume (defined as the average of raw XCO_2 retrievals within $\mu \pm 2\sigma$) minus

95 the surrounding background concentration (derived as the average of raw XCO_2 retrievals outside 2σ) is larger than the standard deviation of the background values within 200 km. Only the cases that pass these two filtering criteria are finally identified as the XCO_2 local enhancements in this study.

2.3 Gaussian plume model

We use the Gaussian plume model (Bovensmann et al., 2010) to attribute the observed XCO_2 enhancement to a neighbor

100 cluster of emission sources. We simulate the sum of XCO_2 plumes generated by each point source and each emission grid cell from the MEIC inventory within 50 km of the studied OCO-2 track with equations:

$$V = \sum_{\in 50km} \frac{F}{\sqrt{2\pi} \cdot a \cdot z^{0.894} \cdot u} e^{-\frac{1}{2}\left(\frac{n}{a \cdot z^{0.894}}\right)^2} \tag{2}$$

$$XCO_2 = V \cdot \frac{M_{air}}{M_{CO2}} \cdot \frac{g}{P_{surf} - w \cdot g} \cdot 1000 \tag{3}$$

where V is the CO_2 vertical column (g m^{-2}) downwind of the emission sources, F is the emission rate (g s^{-1}), u is the wind

105 speed (m s^{-1}), z is the along-wind distance (km), n is the across-wind distance (m), and a is the atmospheric stability parameter. Equation (3) converts V (g m^{-2}) to XCO_2 (ppm), where M is the molecular weight (kg mol^{-1}), g is the gravitational acceleration (m s^{-2}), P_{surf} is the surface pressure (Pa), and w is the total column water vapor (kg m^{-2}).

F is derived from the MEIC emission inventory (Zheng et al., 2018b), including both point sources and 0.1°×0.1° area source emissions. Each grid cell of area sources is used as a point source in Equation (2). u is the average wind at 1000, 975, and 950

110 hPa to approximate the wind below 500 m (Beirle et al., 2011) at the time of the OCO-2 overpass, derived from the ERA5 reanalysis data (C3S, 2017). In the presence of relief, the average of the pressure-level winds is weighted towards the surface. a is a function of the atmospheric stability condition (Martin, 1976) determined by both the 10-m wind speed and the incoming solar radiation (Seinfeld and Pandis, 2006). Wind, solar radiation, and P_{surf} are all derived from the ERA5 reanalysis dataset (C3S, 2017), and w is adopted from the OCO-2 files.

115 ## 2.4 Cross-sectional CO_2 flux estimate

We relate each satellite observed XCO_2 enhancement to anthropogenic emission sources within 50 km using the Gaussian plume model. We visually inspect the observed and modeled XCO_2 and further select the ones that exhibit a single and isolated CO_2 plume to attribute the plume to a neighbor cluster of emission sources and estimate the corresponding cross-sectional CO_2 fluxes. We remove the linear background from the fitted curve of Equation (1) and calculate the area under the remaining fitted

120 curve to derive the CO_2 line density (ppm m), which can be converted to the unit of g m^{-1} through Equation (3). The errors in

the CO_2 line densities are those of the area under the fitted curve, mainly driven by the random errors of the XCO_2 retrievals and also by the Equation (1) that is not a perfect representation of actual CO_2 plumes. The standard error statistics for each parameter in Equation (1) are obtained from the weighted nonlinear least-squares fitting and propagated to calculate the uncertainties of the area under the fitted curve.

The CO_2 line densities are multiplied by the wind speed (m s^{-1}) in the direction normal to the OCO-2 tracks at the location of the plume peak to estimate cross-sectional CO_2 fluxes (g s^{-1}). The average wind below 500 m is used like in Equation (2). To reduce the errors in the wind direction, we allow rotation of the wind direction within 45° on each side of the ERA5 local wind direction to maximize the spatial correlation between the Gaussian plume-modeled and the OCO-2-observed XCO_2 according to Nassar et al. (2017). The derived cross-sectional CO_2 fluxes approximately represent upwind source emissions under steady-state atmospheric conditions, while changes in the atmospheric stability (e.g., strong turbulent diffusion) could make the cross-sectional flux diverge from the source emissions (Varon et al., 2018; Reuter et al., 2019).

3 Results

3.1 CO_2 emission plumes seen by satellite

The identification of CO_2 emission plumes crossed by the satellite field of view starts with the search for XCO_2 local enhancements. These are defined as XCO_2 peaks above the background along the thin OCO-2 tracks. As shown in Fig. 1, we have identified a total of 6,565 OCO-2 ground tracks over or around China between September 2014 and August 2019, with an even share between the cold-season (from September to February, 47%) and the warm-season ones (from March to August, 53%). We find 49,322 cases with local XCO_2 enhancements that exceed 2 sigmas above the local average in a 200 km-wide moving window along the satellite tracks. However, 97% of these XCO_2 enhancements are removed after evaluation of the integrity of the plume section and of the spatial variation of surrounding background retrievals, leaving only 1,439 XCO_2 cases as potent candidates for retrieving emissions.

The second step consists in attempting to attribute the observed 1,439 CO_2 enhancements to nearby human emission sources. Only 370 of the 1,439 XCO_2 local enhancements can be related to emission sources in the MEIC dataset using the Gaussian plume model within a 50-km upwind distance from each OCO-2 ground track. The other cases that reveal XCO_2 enhancement but no nearby emission sources within 50 km upwind are probably due to either OCO-2 XCO_2 retrieval errors at local scales, or sources missing in MEIC, or transport of CO_2 over a longer distance (Parazoo et al., 2011).

The third step is the quantification of cross-sectional CO_2 fluxes within the satellite observed CO_2 plumes. Only 60 of the 370 cases correspond to single isolated CO_2 plumes within a 200 km-wide window, which allows unambiguous attribution to an emission site or cluster. One reason why we reject the other 310 cases is that they have two or more individual plumes, partially overlapping or separated. Some of the rejected cases also lack observation data of good quality (*xco2_quality_flag* equals 0) at a distance of several tens of kilometers due to significant retrieval errors in the local satellite observations.

The data filtering process retains more cold-season observations (55%) than warm-season ones, in particular after the first step (52% cases are from the cold season after the first step), due to favorable meteorological patterns during the cold season. Although the total number of selected cases is small, it is several times larger than in previous studies that only focused on large cities and large power plants in different locations of the world (Nassar et al., 2017; Reuter et al., 2019; Wu et al., 2020). The finally selected 60 cases include both densely populated urban areas (33 cases) and small industrial areas (27 cases) that gather many industrial plants. The peak height of XCO_2 enhancement in the plumes ($A/(\sigma\sqrt{2\pi})$ in Equation (1)) is within 1.1–6.0 µmol mol^{-1} (abbreviated as ppm) above the average local background and 2–7 times higher than the standard deviation of background levels within 200 km. The width of observed CO_2 plumes, defined as the full width at half maximum of peak height, is estimated between 2.2 and 61.2 km.

3.2 Quantifying CO_2 emissions: one city example

Figure 2 presents one example of the 60 selected cases. The emitter here is the city Anshan that has about 1.5 million inhabitants. On October 17th 2016, CO_2 emissions from Anshan were blown southward by a 7.1 m s^{-1} wind at the OCO-2 overpass time and generated an XCO_2 local enhancement larger than 2 ppm (Fig. 2). At about 13:30 local time, OCO-2 flew over the east of China (Fig. 2a), crossed the CO_2 plume transported from Anshan, and successfully observed the local enhancement near the southernmost part of the OCO-2 ground track (Fig. 2b).

We plot the XCO_2 retrieval data (grey dots in Fig. 2c) along the satellite ground track, the plot window of which is centered at the highest XCO_2 value in the CO_2 plume. We first fit the black curve ($R^2 = 0.4$) based on Equation (1) to depict the CO_2 plume transect. The local background is represented by a straight line $-2.6\mathrm{E}{-}3{\cdot}x + 402.1$ that approximates a flat background of 402.1 ppm. Then we subtract the background line from both the XCO_2 data and the fitted black curve to obtain the net enhancement of XCO_2 above the local background (pink dots and red curve in Fig. 2d). The maximum XCO_2 net enhancement (peak height of the red curve) is 2.4 ppm and the plume width is 15.0 km. The CO_2 line density is estimated as 0.60 ± 0.04 t-CO_2 m^{-1} (central estimate $\pm$ 1σ) by computing the area under the red curve (the orange shade in Fig. 2d). The uncertainty is mainly caused by random errors of the single XCO_2 retrievals.

The CO_2 line density derived from the satellite retrievals is further multiplied by the wind speed in the normal direction to the OCO-2 track to quantify the cross-sectional CO_2 flux. We use the average wind below 500 m from the ERA5 reanalysis data. The ceiling height of 500 m is comparable to the maximum height that smoke plumes from power plants and industrial plants typically reach. The wind direction around Anshan is optimized according to Nassar et al. (2017) and is shifted by 1° in this case to maximize the spatial correlation between the satellite-observed (Fig. 2d) and the model-simulated (Fig. 2e) XCO_2 enhancements. The wind speed in the normal direction to the OCO-2 track is then estimated as 2.6 m s^{-1} at the location of the maximum XCO_2 value (Fig. 2b). The CO_2 hourly flux at the satellite overpassing time is finally estimated as 5.7 ± 1.2 kt-CO_2 h^{-1}, considering uncertainties both in the CO_2 line density and in the wind speed.

The satellite observed CO_2 plume can be traced back to anthropogenic emission sources located in the urbanized area of the Anshan city by the Gaussian plume model combined with the local emission map given by the MEIC inventory. We use

185   monthly, weekly, and diurnal emission time profiles by region and by source sector from MEIC to split the annual emission
       totals reported by MEIC to hourly emission rates during the satellite overpass. The MEIC hourly emission rate of Anshan is
       6.4 ± 1.9 kt-CO_2 h^{-1}, which is close to the satellite-based inversion estimate.

3.3 CO_2 emission estimates for 60 cases in China

       We quantify the CO_2 emissions corresponding to the 60 CO_2 plumes selected from the five-year OCO-2 archive. These
190   represent 46 different urban areas or industrial regions in China. There are 14 regions whose emission plumes were observed
       twice in our selection of the satellite data. The 60 CO_2 plumes present CO_2 line densities between 0.1 and 2.8 t-CO_2 m^{-1}, and
       hourly CO_2 fluxes at the time of the satellite overpass are estimated within the range of 0.3–16.0 kt-CO_2 h^{-1} with the 1σ
       uncertainties of 20–30%. The larger sources tend to present lower relative uncertainties, because a larger XCO_2 enhancement
       makes it easier to separate a plume from its background, and is thus more easily observed by the satellite. The inversions that
195   estimate CO_2 emissions larger than 4 kt-CO_2 h^{-1} tend to constrain their relative uncertainties below 25%.
       We compare the satellite-based CO_2 hourly fluxes to the corresponding source emissions given by MEIC (Fig. 3), after
       applying emission time profiles to transform MEIC annual emissions into hourly emissions at the time of satellite overpass.
       Although the point source based MEIC emissions data is only for the year 2013, China's countrywide emissions remained
       stable between 2013 and 2017 and marginally grew only after 2017 (Friedlingstein et al., 2019). The satellite-based and MEIC
200   estimated emissions are broadly consistent within a factor of two (solid dots in Fig. 3) with comparable uncertainties for the
       same individual estimates. The average of satellite-based estimates is 27.1% higher than the MEIC values in the cold season
       (solid blue dots in Fig. 3), while 5.2% lower in the warm season (solid red dots in Fig. 3).
       The differences in the results between cold and warm seasons could be due to uncertainties in the emission estimate methods
       of both our OCO-2 based inversion and the MEIC inventory. The satellite-based larger estimates in the cold season could be
205   partially due to the fact that human respiration contributes to urban CO_2 fluxes while not included in the MEIC inventory of
       fossil fuel and cement emissions. We make a rough estimate of the metabolic CO_2 release by multiplying an emission factor
       of 0.52 t-CO_2 yr^{-1} person^{-1} (Prairie and Duarte, 2007) by the population living in each emitting area. The results suggest that
       human metabolic CO_2 emissions explain 8% of the larger satellite-based emission estimates on average in the cold season. The
       remaining difference could be due to the assumption that the 0–500 m average wind speed is representative of the transport
210   wind in the plume diffusion, the natural processes like plant respiration, or the slight growth of fossil fuel emissions since
       2013, but could also reflect some bias in the MEIC estimates. In the warm season, despite human respiration emissions, the
       satellite-based inversions give lower emission estimates possibly due to the carbon uptake by plants damping the XCO_2
       enhancements (Mitchell et al., 2018), which makes anthropogenic emission signals not easily separated from the background
       in the satellite-based inversions.
215   The uncertainties in the satellite-based emission estimates are driven by those of the local wind field and of the CO_2 line density
       derived from the XCO_2 retrievals. We reduce the errors in wind directions and consequently increase the R^2 of the linear
       correlation between satellite- and MEIC-based emission estimates across emitting areas from 0.37 (open dots) to 0.50 (solid

dots) as shown in Fig. 3. The magnitude of the wind speed uncertainty, typically considered 10–20% (Nassar et al., 2017; Varon et al., 2018; Reuter et al., 2019), is comparable to the uncertainty in the satellite-based CO_2 line densities (3–23% for

220 the 60 emission plumes). In high wind-speed conditions, the CO_2 plumes are spread more quickly and thus cause smaller local enhancements, which weakens the signal of XCO_2 and causes larger uncertainties in the estimate of CO_2 line densities. Generally, our estimates reach lower relative uncertainties for larger emission cities under lower wind speeds.

3.4 Comparison with global bottom-up inventories

We extrapolate the satellite-based CO_2 hourly fluxes to annual total fluxes using emission time profiles, and compare them to

225 two global bottom-up emission maps: ODIAC (Oda and Maksyutov, 2015, Oda et al., 2018) and EDGAR (Janssens-Maenhout et al., 2019). We use the cases between the years 2014 and 2018 when both inventories are available, and extract CO_2 emissions over each satellite-observed emitting area from the emission maps (Fig. 4). For the areas observed by the satellite in different years, we compute annual values from the corresponding inversions and average them for the comparison with ODIAC and EDGAR.

230 For individual estimates, ODIAC (Figs. 4b) and EDGAR (Figs. 4c) are broadly consistent with the annual budgets from the satellite-based inversions, but the fit is slightly better in the case of EDGAR. The large discrepancies are not surprising since global emission inventories typically involve large uncertainties at city scales (Gately and Hutyra, 2017; Gurney et al., 2019), because they disaggregate national emissions to gridded maps with simple proxies like population or nighttime light in the countries like China where they lack detailed direct local information. Only large power plants have exact geographic locations

235 (from the CARMA global database (Wheeler and Ummel, 2008)), in principle, but not all of the industrial plants like MEIC. ODIAC uses nightlights to disaggregate national emission estimates to grid cells, which may lead to an underestimation of road emissions in cities (Gately and Hutyra, 2017) and a misplacing of industrial emissions. EDGAR relies on point source locations to allocate emissions in space while it still suffers from missing local information in China, and gridded population maps have to be used instead. Such an emission mapping approach overestimates emissions over densely populated cities in

240 China (Zheng et al., 2017), because the industry plants, the primary CO_2 emission sources in China, are located far away from densely populated urban areas. The MEIC inventory estimates industrial emissions at the facility scale, transport emissions at the county scale, and residential emissions at the provincial scale, which can achieve better spatial accuracy in emissions estimates than the global emission inventories.

The sum of the emissions from the satellite-observed areas reaches 1.25 Gt CO_2 yr^{-1} (Fig. 4a), accounting for approximately

245 13% of the mainland China's total emissions. The corresponding bottom-up estimates from ODIAC, EDGAR, and MEIC are 1.13, 1.38, and 1.17 Gt CO_2 yr^{-1}, respectively. ODIAC emissions are 9.6% lower than the satellite-based estimates while EDGAR emissions are 10.4% higher. The slight growth of the emissions from 2014 to 2018 (documented in, e.g., EDGAR) could alone explain mostly the 6% lower value for MEIC (valid for the year 2013) than the satellite estimate. Overall, EDGAR matches the individual estimates from the satellite-based inversions better than ODIAC for the 13% of mainland China's CO_2

250 emissions that are observed by the satellite. However, both of these two global emission inventories reveal large uncertainties in emission estimates for individual areas as shown in Figs. 4b and 4c.

4. Conclusions

We developed a novel objective approach to quantify local anthropogenic CO_2 emissions from the OCO-2 XCO_2 satellite retrievals. The key of this method is a conservative selection of the satellite data that can be safely exploited for emission
255 quantification. It also depends on the wind information and the information about the locations of human emission sources in the upwind vicinity of the selected OCO-2 tracks. Future developments could aim at refining the stringent data selection, or at improving the estimation of wind speed or the description of the plume footprint, for instance using detailed regional atmospheric transport models but the current simplicity of our approach makes it easily applicable everywhere over the globe in principle. Our first regional analysis over mainland China suggests that 13% of its CO_2 human emissions can be observed
260 and constrained, to some extent, by five years of retrieval data from the OCO-2, a satellite instrument not designed for this task. The satellite-based emission inversion results are broadly consistent (R^2=0.50, meaning we agree on broad classes of emitters) with the reliable point source-based MEIC regional inventory despite our simple modeling of the plume and of its background, and despite possible biases due to local non-fossil fuel emissions or local sinks that contribute to the plume intensity. We also use the satellite-based estimates as a rough independent evaluation of two global bottom-up inventories,
265 ODIAC and EDGAR.

There is still a large gap between what the satellite can see and what the National Greenhouse Gas Inventory reports submitted to the United Nations Framework Convention on Climate Change (UNFCCC), mentioned at the start of the introduction. The former is made of specific emission plumes linked to recent emission events without any sectoral distinction within the plume. The latter is made of the country- and annual-scale emission values assigned to specific human-caused source/sink categories.
270 The exhaustiveness of the MEIC inventory, which involved detailed analysis of the fine spatial and temporal emission patterns, allowed us to bridge most of this gap for a time period when Chinese emissions did not vary much, but few countries have such a detailed geospatial inventory of their emissions and are able to update it timely for such a task. We also acknowledge the limitations of the emission temporal profiles even from the detailed MEIC inventory. The sparse sampling of the OCO-2 instrument, despite the good precision of individual soundings, will partly be overcome by the next-generation of CO_2-
275 dedicated imagery satellites, such as the CO_2 Monitoring mission (CO2M) in Europe (Clery, 2019; Janssens-Maenhout et al., 2020) and the Geostationary Carbon Cycle Observatory (GeoCarb) in the U.S. (Moore III et al., 2018) that will have denser spatial coverage. However, their measurement principle still relies on sunlight and will prevent us from well sampling the emission diurnal cycle. The need for a good knowledge of the emission space-time patterns (not only the emission values) will therefore remain for the comparison between the national inventories and the satellite-based estimates. However, for countries
280 with less advanced CO_2 inventory infrastructures (typically non-Annex I parties to UNFCCC), we could also envisage an incremental approach where both bottom-up and top-down estimates are developed together in parallel.

Data availability

The version 9r of the OCO-2 bias-corrected XCO_2 retrievals were downloaded from the data archive maintained at the NASA Goddard Earth Science Data and Information Services Center (https://oco2.gesdisc.eosdis.nasa.gov/data/s4pa/OCO2_DATA/OCO2_L2_Lite_FP.9r/, last access: 12 February 2020; Kiel et al., 2019). The ERA5 reanalysis data were acquired from the Copernicus Climate Change Service Climate Data Store (https://cds.climate.copernicus.eu/, last access: 12 February 2020; C3S, 2017).

Author contributions

BZ, FC, and PC designed the study. BZ processed the observational data and estimated the CO_2 fluxes from the satellite observations. BZ prepared the paper with contributions from all coauthors.

Competing interests

The authors declare that they have no conflict of interest.

Acknowledgements

The OCO-2 retrievals were produced by the OCO-2 project at the Jet Propulsion Laboratory, California Institute of Technology, and obtained from the OCO-2 data archive maintained at the NASA Goddard Earth Science Data and Information Services Center.

References

Beirle, S., Boersma, K. F., Platt, U., Lawrence, M. G., and Wagner, T.: Megacity Emissions and Lifetimes of Nitrogen Oxides Probed from Space, Science, 333, 1737-1739, doi: 10.1126/science.1207824, 2011.

Bovensmann, H., Buchwitz, M., Burrows, J. P., Reuter, M., Krings, T., Gerilowski, K., Schneising, O., Heymann, J., Tretner, A., and Erzinger, J.: A remote sensing technique for global monitoring of power plant CO_2 emissions from space and related applications, Atmos. Meas. Tech., 3, 781-811, doi: 10.5194/amt-3-781-2010, 2010.

Broquet, G., Bréon, F. M., Renault, E., Buchwitz, M., Reuter, M., Bovensmann, H., Chevallier, F., Wu, L., and Ciais, P.: The potential of satellite spectro-imagery for monitoring CO_2 emissions from large cities, Atmos. Meas. Tech., 11, 681-708, doi: 10.5194/amt-11-681-2018, 2018.

Chevallier, F.: Comment on "Contrasting carbon cycle responses of the tropical continents to the 2015–2016 El Niño", Science, 362, eaar5432, doi: 10.1126/science.aar5432, 2018.

Clery, D.: Space budget boost puts Europe in lead to monitor carbon from space, Science, 2019.

Copernicus Climate Change Service (C3S) (2017): ERA5: Fifth generation of ECMWF atmospheric reanalyses of the global
310   climate, Copernicus Climate Change Service Climate Data Store (CDS), https://cds.climate.copernicus.eu/cdsapp#!/home
(accessed in Aug 2019).

Eldering, A., Wennberg, P. O., Crisp, D., Schimel, D. S., Gunson, M. R., Chatterjee, A., Liu, J., Schwandner, F. M., Sun, Y.,
O'Dell, C. W., Frankenberg, C., Taylor, T., Fisher, B., Osterman, G. B., Wunch, D., Hakkarainen, J., Tamminen, J., and Weir,
B.: The Orbiting Carbon Observatory-2 early science investigations of regional carbon dioxide fluxes, Science, 358, eaam5745,
315   doi: 10.1126/science.aam5745, 2017.

Friedlingstein, P., Jones, M. W., O'Sullivan, M., Andrew, R. M., Hauck, J., Peters, G. P., Peters, W., Pongratz, J., Sitch, S., Le
Quéré, C., Bakker, D. C. E., Canadell, J. G., Ciais, P., Jackson, R. B., Anthoni, P., Barbero, L., Bastos, A., Bastrikov, V.,
Becker, M., Bopp, L., Buitenhuis, E., Chandra, N., Chevallier, F., Chini, L. P., Currie, K. I., Feely, R. A., Gehlen, M., Gilfillan,
D., Gkritzalis, T., Goll, D. S., Gruber, N., Gutekunst, S., Harris, I., Haverd, V., Houghton, R. A., Hurtt, G., Ilyina, T., Jain, A.
320   K., Joetzjer, E., Kaplan, J. O., Kato, E., Klein Goldewijk, K., Korsbakken, J. I., Landschützer, P., Lauvset, S. K., Lefèvre, N.,
Lenton, A., Lienert, S., Lombardozzi, D., Marland, G., McGuire, P. C., Melton, J. R., Metzl, N., Munro, D. R., Nabel, J. E. M.
S., Nakaoka, S. I., Neill, C., Omar, A. M., Ono, T., Peregon, A., Pierrot, D., Poulter, B., Rehder, G., Resplandy, L., Robertson,
E., Rödenbeck, C., Séférian, R., Schwinger, J., Smith, N., Tans, P. P., Tian, H., Tilbrook, B., Tubiello, F. N., van der Werf, G.
R., Wiltshire, A. J., and Zaehle, S.: Global Carbon Budget 2019, Earth Syst. Sci. Data, 11, 1783-1838, doi: 10.5194/essd-11-
325   1783-2019, 2019.

Gately, C. K., and Hutyra, L. R.: Large Uncertainties in Urban-Scale Carbon Emissions, J. Geophys. Res. Atmos., 122, 11,242-
211,260, doi: 10.1002/2017jd027359, 2017.

Gurney, K. R., Liang, J., O'Keeffe, D., Patarasuk, R., Hutchins, M., Huang, J., Rao, P., and Song, Y.: Comparison of Global
Downscaled Versus Bottom-Up Fossil Fuel CO_2 Emissions at the Urban Scale in Four U.S. Urban Areas, J. Geophys. Res.
330   Atmos., 124, 2823-2840, doi: 10.1029/2018jd028859, 2019.

IPCC (Intergovernmental Panel on Climate Change): 2019 Refinement to the 2006 IPCC Guidelines for National Greenhouse
Gas Inventories, https://www.ipcc-nggip.iges.or.jp/public/2019rf/, 2019.

Janssens-Maenhout, G., Crippa, M., Guizzardi, D., Muntean, M., Schaaf, E., Dentener, F., Bergamaschi, P., Pagliari, V.,
Olivier, J. G. J., Peters, J. A. H. W., van Aardenne, J. A., Monni, S., Doering, U., Petrescu, A. M. R., Solazzo, E., and Oreggioni,
335   G. D.: EDGAR v4.3.2 Global Atlas of the three major greenhouse gas emissions for the period 1970–2012, Earth Syst. Sci.
Data, 11, 959-1002, doi: 10.5194/essd-11-959-2019, 2019.

Janssens-Maenhout, G., Pinty, B., Dowell, M., Zunker, H., Andersson, E., Balsamo, G., Bézy, J.-L., Brunhes, T., Bösch, H.,
Bojkov, B., Brunner, D., Buchwitz, M., Crisp, D., Ciais, P., Counet, P., Dee, D., Denier van der Gon, H., Dolman, H.,
Drinkwater, M., Dubovik, O., Engelen, R., Fehr, T., Fernandez, V., Heimann, M., Holmlund, K., Houweling, S., Husband, R.,
340   Juvyns, O., Kentarchos, A., Landgraf, J., Lang, R., Löscher, A., Marshall, J., Meijer, Y., Nakajima, M., Palmer, P. I., Peylin,
P., Rayner, P., Scholze, M., Sierk, B., Tamminen, J., and Veefkind, P.: Towards an operational anthropogenic CO_2 emissions

monitoring and verification support capacity, Bulletin of the American Meteorological Society, doi: 10.1175/bams-d-19-0017.1, 2020.

Kiel, M., O'Dell, C. W., Fisher, B., Eldering, A., Nassar, R., MacDonald, C. G., and Wennberg, P. O.: How bias correction
345   goes wrong: measurement of XCO_2 affected by erroneous surface pressure estimates, Atmos. Meas. Tech., 12, 2241-2259, doi: 10.5194/amt-12-2241-2019, 2019.

Kort, E. A., Frankenberg, C., Miller, C. E., and Oda, T.: Space-based observations of megacity carbon dioxide, Geophys. Res. Lett., 39, doi: 10.1029/2012gl052738, 2012.

Kuhlmann, G., Broquet, G., Marshall, J., Clément, V., Löscher, A., Meijer, Y., and Brunner, D.: Detectability of CO_2 emission
350   plumes of cities and power plants with the Copernicus Anthropogenic CO_2 Monitoring (CO2M) mission, Atmos. Meas. Tech., 12, 6695-6719, doi: 10.5194/amt-12-6695-2019, 2019.

Labzovskii, L. D., Jeong, S.-J., and Parazoo, N. C.: Working towards confident spaceborne monitoring of carbon emissions from cities using Orbiting Carbon Observatory-2, Remote Sensing of Environment, 233, 111359, doi: 10.1016/j.rse.2019.111359, 2019.

355   Liu, J., Bowman, K. W., Schimel, D. S., Parazoo, N. C., Jiang, Z., Lee, M., Bloom, A. A., Wunch, D., Frankenberg, C., Sun, Y., O'Dell, C. W., Gurney, K. R., Menemenlis, D., Gierach, M., Crisp, D., and Eldering, A.: Contrasting carbon cycle responses of the tropical continents to the 2015–2016 El Niño, Science, 358, eaam5690, doi: 10.1126/science.aam5690, 2017.

Martin, D. O.: Comment On"The Change of Concentration Standard Deviations with Distance", Journal of the Air Pollution Control Association, 26, 145-147, doi: 10.1080/00022470.1976.10470238, 1976.

360   Mitchell, L. E., Lin, J. C., Bowling, D. R., Pataki, D. E., Strong, C., Schauer, A. J., Bares, R., Bush, S. E., Stephens, B. B., Mendoza, D., Mallia, D., Holland, L., Gurney, K. R., and Ehleringer, J. R.: Long-term urban carbon dioxide observations reveal spatial and temporal dynamics related to urban characteristics and growth, Proc. Natl. Acad. Sci., 115, 2912-2917, doi: 10.1073/pnas.1702393115, 2018.

Moore III, B., Crowell, S. M. R., Rayner, P. J., Kumer, J., O'Dell, C. W., O'Brien, D., Utembe, S., Polonsky, I., Schimel, D.,
365   and Lemen, J.: The Potential of the Geostationary Carbon Cycle Observatory (GeoCarb) to Provide Multi-scale Constraints on the Carbon Cycle in the Americas, Frontiers in Environmental Science, 6, doi: 10.3389/fenvs.2018.00109, 2018.

Nassar, R., Hill, T. G., McLinden, C. A., Wunch, D., Jones, D. B. A., and Crisp, D.: Quantifying CO_2 Emissions From Individual Power Plants From Space, Geophys. Res. Lett., 44, 10,045-010,053, doi: 10.1002/2017gl074702, 2017.

O'Brien, D. M., Polonsky, I. N., Utembe, S. R., and Rayner, P. J.: Potential of a geostationary geoCARB mission to estimate
370   surface emissions of CO_2, CH_4 and CO in a polluted urban environment: case study Shanghai, Atmos. Meas. Tech., 9, 4633-4654, doi: 10.5194/amt-9-4633-2016, 2016.

Oda, T., and Maksyutov, S.: ODIAC Fossil Fuel CO_2 Emissions Dataset (ODIAC2019), Center for Global Environmental Research, National Institute for Environmental Studies, doi:10.17595/20170411.001, 2015. (accessed on 2019/12/20)

Oda, T., Maksyutov, S., and Andres, R. J.: The Open-source Data Inventory for Anthropogenic CO_2, version 2016 (ODIAC2016): a global monthly fossil fuel CO_2 gridded emissions data product for tracer transport simulations and surface flux inversions, Earth Syst. Sci. Data, 10, 87-107, doi: 10.5194/essd-10-87-2018, 2018.

Palmer, P. I., Feng, L., Baker, D., Chevallier, F., Bösch, H., and Somkuti, P.: Net carbon emissions from African biosphere dominate pan-tropical atmospheric CO_2 signal, Nature Communications, 10, 3344, doi: 10.1038/s41467-019-11097-w, 2019.

Parazoo, N. C., Denning, A. S., Berry, J. A., Wolf, A., Randall, D. A., Kawa, S. R., Pauluis, O., and Doney, S. C.: Moist synoptic transport of CO_2 along the mid-latitude storm track, Geophys. Res. Lett., 38, doi: 10.1029/2011gl047238, 2011.

Prairie, Y. T., and Duarte, C. M.: Direct and indirect metabolic CO_2 release by humanity, Biogeosciences, 4, 215-217, doi: 10.5194/bg-4-215-2007, 2007.

Reuter, M., Buchwitz, M., Schneising, O., Krautwurst, S., O'Dell, C. W., Richter, A., Bovensmann, H., and Burrows, J. P.: Towards monitoring localized CO_2 emissions from space: co-located regional CO_2 and NO_2 enhancements observed by the OCO-2 and S5P satellites, Atmos. Chem. Phys., 19, 9371-9383, doi: 10.5194/acp-19-9371-2019, 2019.

Seinfeld, J. H., and Pandis, S. N.: Atmospheric chemistry and physics: from air pollution to climate change, John Wiley & Sons, Inc., Hoboken, p. 750, 2006.

Schwandner, F. M., Gunson, M. R., Miller, C. E., Carn, S. A., Eldering, A., Krings, T., Verhulst, K. R., Schimel, D. S., Nguyen, H. M., Crisp, D., O'Dell, C. W., Osterman, G. B., Iraci, L. T., and Podolske, J. R.: Spaceborne detection of localized carbon dioxide sources, Science, 358, eaam5782, doi: 10.1126/science.aam5782, 2017.

Varon, D. J., Jacob, D. J., McKeever, J., Jervis, D., Durak, B. O. A., Xia, Y., and Huang, Y.: Quantifying methane point sources from fine-scale satellite observations of atmospheric methane plumes, Atmos. Meas. Tech., 11, 5673-5686, doi: 10.5194/amt-11-5673-2018, 2018.

Wang, Y., Broquet, G., Bréon, F. M., Lespinas, F., Buchwitz, M., Reuter, M., Meijer, Y., Loescher, A., Janssens-Maenhout, G., Zheng, B., and Ciais, P.: PMIF v1.0: an inversion system to estimate the potential of satellite observations to monitor fossil fuel CO_2 emissions over the globe, Geosci. Model Dev. Discuss., 2020, 1-27, doi: 10.5194/gmd-2019-326, 2020.

Wheeler, D., and Ummel, K.: Calculating Carma: Global Estimation of CO_2 Emissions from the Power Sector, Available at SSRN: https://ssrn.com/abstract=1138690 or http://dx.doi.org/10.2139/ssrn.1138690, 2008.

Worden, J. R., Doran, G., Kulawik, S., Eldering, A., Crisp, D., Frankenberg, C., O'Dell, C., and Bowman, K.: Evaluation and attribution of OCO-2 XCO_2 uncertainties, Atmos. Meas. Tech., 10, 2759-2771, doi: 10.5194/amt-10-2759-2017, 2017.

Wu, D., Lin, J., Oda, T., and Kort, E.: Space-based quantification of per capita CO_2 emissions from cities, Environ. Res. Lett 2020.

UNFCCC (United Nation Framework Convention on Climate Change): Decision 18/CMA.1 Modalities, procedures and guidelines for the transparency framework for action and support referred to in Article 13 of the Paris Agreement, FCCC/PA/CMA/2018/Add.2, 2018.

Zheng, B., Zhang, Q., Tong, D., Chen, C., Hong, C., Li, M., Geng, G., Lei, Y., Huo, H., and He, K.: Resolution dependence of uncertainties in gridded emission inventories: a case study in Hebei, China, Atmos. Chem. Phys., 17, 921-933, doi: 10.5194/acp-17-921-2017, 2017.

410   Zheng, B., Tong, D., Li, M., Liu, F., Hong, C., Geng, G., Li, H., Li, X., Peng, L., Qi, J., Yan, L., Zhang, Y., Zhao, H., Zheng, Y., He, K., and Zhang, Q.: Trends in China's anthropogenic emissions since 2010 as the consequence of clean air actions, Atmos. Chem. Phys., 18, 14095-14111, doi: 10.5194/acp-18-14095-2018, 2018a.

Zheng, B., Zhang, Q., Davis, S. J., Ciais, P., Hong, C., Li, M., Liu, F., Tong, D., Li, H., and He, K.: Infrastructure Shapes Differences in the Carbon Intensities of Chinese Cities, Environ. Sci. Technol., doi: 10.1021/acs.est.7b05654, 2018b.

Zheng, T., Nassar, R., and Baxter, M.: Estimating power plant CO_2 emission using OCO-2 XCO_2 and high resolution WRF-415   Chem simulations, Environ. Res. Lett., 14, 085001, doi: 10.1088/1748-9326/ab25ae, 2019.
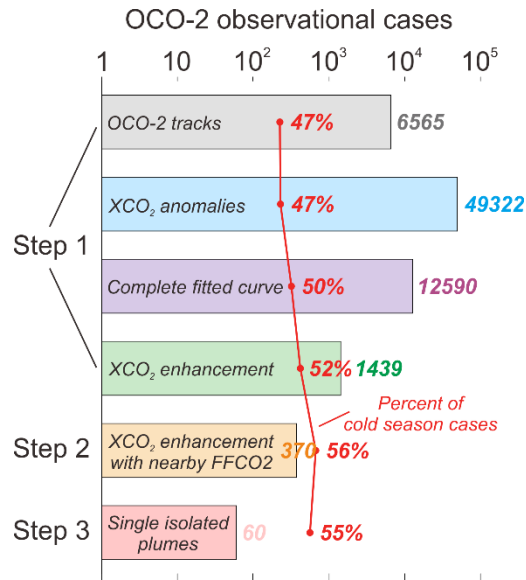
Figure 1: OCO-2 XCO₂ observational cases contained in each processing step. Step 1 starts from 6,565 OCO-2 tracks around and over China between September 2014 and August 2019 (grey bar) and finds 49,322 XCO2 anomalies along the OCO-2 tracks (blue bar). 12,590 anomalies (purple bar) and their surrounding data points within a 200 km-wide window can be fitted by a complete nonlinear curve using Equation (1), of which 1,439 XCO2 anomalies (green bar) are identified as local enhancement significantly higher than the background. Step 2 uses the Gaussian plume model to select 370 XCO2 enhancements (yellow bar) that can be traced back to upwind fossil fuel emission sources within 50 km. In step 3, we finally select the 60 cases with single isolated CO2 plumes to quantify the CO2 emissions. The red curve shows the percentage of cold-season observational cases in each bar. The detail of each step is described in Sect. 2.
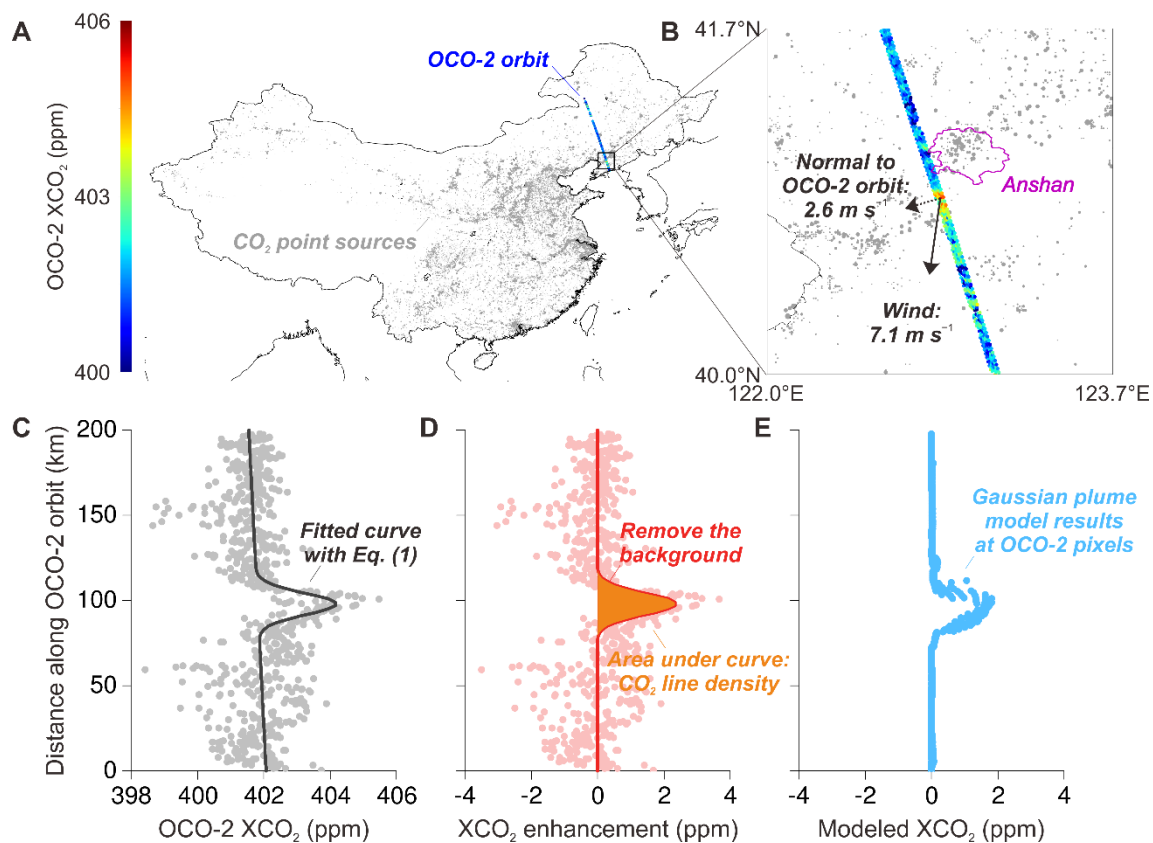
Figure 2: Quantification of CO₂ emissions from Anshan. (A) The OCO-2 orbit on October 17th 2016 is plotted on the map of MEIC emission point sources. (B) Zoom in closer to see OCO-2 XCO₂ data, local wind speed, and wind direction. The width of the track is made of eight cross-track OCO-2 footprints. (C) The valid XCO₂ data points (grey dots) plotted along the OCO-2 orbit with a fitted curve (black) based on Equation (1). (D) The XCO₂ enhancement (red dots) above background, the fitted curve (red), and the area under the curve (orange shade). (E) The modeled XCO₂ enhancement (blue dots) by the Gaussian plume model combined with the MEIC emission inventory.
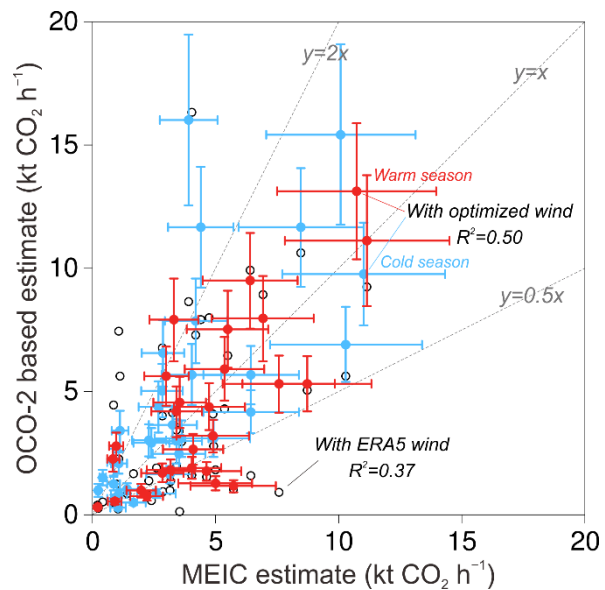
430

Figure 3: Comparison between OCO-2 based and MEIC estimated CO₂ hourly fluxes. Each dot represents one of the 60 plume cases selected in this study, plotted according to the MEIC estimated CO_2 flux (x-axis) and the OCO-2-based estimate (y-axis). The open dots are OCO-2 estimates using the ERA5 wind data, while the solid dots use the optimized wind and distinguish the warm-season (red dots) and the cold-season (blue dots) cases.
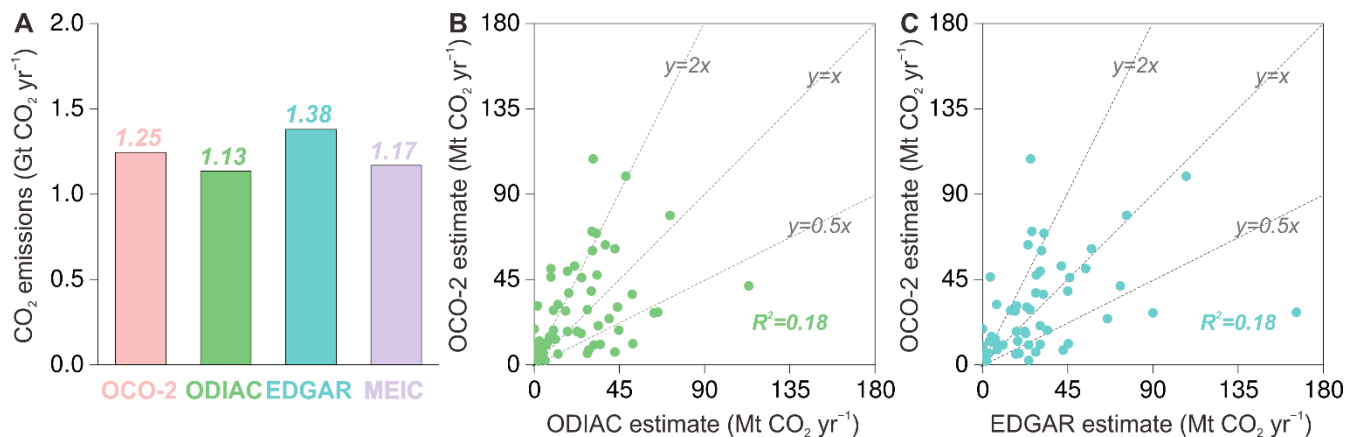
435

Figure 4: Comparing OCO-2 based CO₂ emission estimates with bottom-up inventories. (A) The sum of emissions from the different regions observed by OCO-2 between the years 2014 and 2018, including OCO-2 estimates (scaled up to annual emissions based on MEIC emission time profiles, pink bar), ODIAC (green bar), EDGAR (blue bar), and MEIC (purple bar) estimates. (B) Comparison of regional CO₂ emissions between OCO-2-based (y-axis) and ODIAC estimates (x-axis). (C) Comparison of regional CO₂ emissions between OCO-2-

440   based (y-axis) and EDGAR estimates (x-axis).